Simulation of different path strategies for wire-arc additive manufacturing with Lagrangian finite element methods

R. Israr[1], J. Buhl[1], L. Elze[1], M. Bambach[1]

[1]Brandenburg University of Technology Cottbus–Senftenberg, Chair of Mechanical Design and Manufacturing

1   Introduction

1.1   Additive manufacturing with wire and arc

Established manufacturing processes such as metal forming are suitable for mass production, but for small batch sizes and individualized components, the manufacturing costs rise due to the inevitable tooling costs. For such applications, additive manufacturing (AM) processes, which do not require tooling, and are more suitable for customized and complex parts, are advantageous. Nowadays, wire-arc additive manufacturing (WAAM) that uses the arc welding is considered as one of the most competitive 3D printing technologies for medium to large-scale parts [1]. The wire-arc process builds up the required shape by successively depositing the consumable electrode layer-by-layer.

1.2   Physical phenomena and modelling approaches

Due to the intensive thermal input in the arc-welding process, the product of WAAM may have defects like a high geometrical inaccuracy due to thermal distortions and thermal cracks [2]. These unwanted effects mainly depend on the welding path, the process settings and the cooling behavior. The thermal inputs cause inhomogeneous thermal contraction that leads to mechanical stresses and strains over time [3]. The temperature history during WAAM is highly dependent on the heat transfer coefficient, the heat conduction in the part and radiation to the surrounding.
The welding simulations and the simulations that use welding for making AM components involve phenomena like heat transfer, phase transition, conduction, convection and radiation. Liou et al. used a multi-physics model for AM to investigate heat transfer, distortion and residual stresses [4], Ito et al. investigated the heat generation and weld pool development of gas metal arc welding [5] and Das et al. modelled the wire-arc welding process regarding temperature distributions, residual stresses and plastic deformations [6]. Especially for WAAM the coupling of thermal, mechanical and microstructural solvers is needed [7]. Thus, various temperature dependent effects like distortion, plastic deformation and residual stresses can be calculated. Irregular flow patterns within the weld pool, non-uniform distribution of temperature and inaccurate estimation of weld pool geometry can be predicted. Due to the complexity of the model, difficulties in resolving the large distortions, thermal stresses and residual stresses occur, which leads to large computational time or even to termination of the solver [8–11]. Even the thermal cycles and fluctuation of temperature due to a moving weld source cause diversity in mechanical properties and microstructure [12]. In order to deal with such issues the material properties and the simulation parameters should be carefully chosen and monitored.

1.3   Aim of the investigations

Till now principle investigations of WAAM were carried out, but the influence of the path strategy on the temperature, stress and strain distribution is unknown. This paper shows a WAAM-model in LSDYNA with first results of a benchmark of four path strategies for a simple box. Therefore, the WAAM-process is established for 14 layers (900 sec) and an additional cooling process, which takes 4500 sec. To neglect the evolution of microstructure under cyclic loading, the robust welding steel grade 309-L is used [13]. All statement will be dependend on the boundaries and may change with other boundary conditions.

2 Time and temperature dependent boundary and contact definitions

2.1 Geometrical specifications of the model

A multi-layer FEM model was built in LS-DYNA using thermo-mechanical analysis. With the different path strategies uni-directional, bi-directional, cross-pattern and a spiral path, 14 layers were stacked onto each other to obtain a box (L=81 mm, W=27 mm, and H=22.4 mm). The welding process starts on a 4 mm thick metal plate, whose corners are fixed in the marked direction (*Fig.1*). All beads have the same cross-section with a width of 4.5 mm, a height of 1.6 mm and a pattern-dependent length. For fast thermo-mechanical simulation a mesh with 2 elements in the height and three elements in the width of the bead is used, more precise thermo-mechanical simulations for residual stresses have 3 and 4 elements. In welding direction, the mesh size is 2.25 mm respectively 1.25 mm. For the substrate and the weld beads, the steel grade 309-L is used.
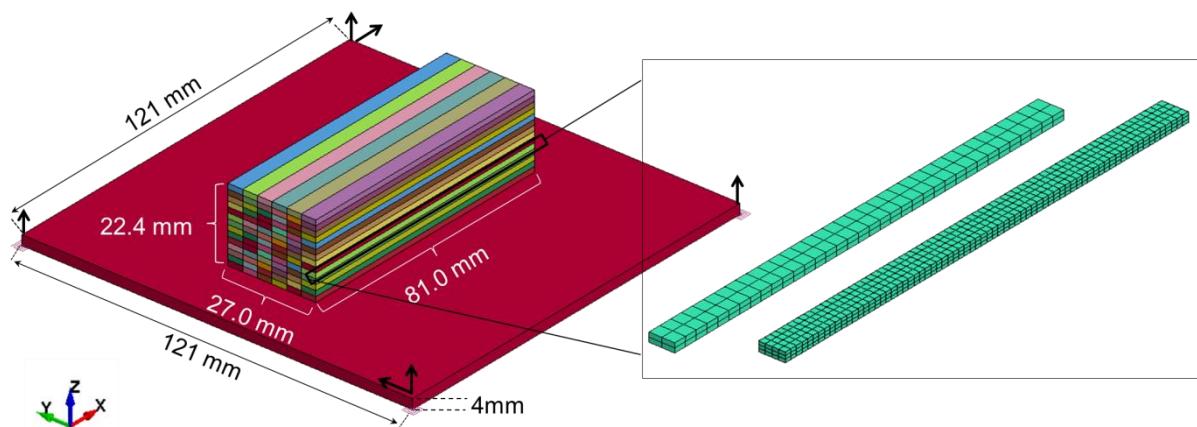
Fig.1: Isometric view of the complete assembly, bold arrows show the constraint directions.

2.2 Material properties of the weld bead

Two material models were used in this work for structural and thermal analysis. The thermal analysis was carried out using ***MAT_Thermal_CWM T07**. The deposition of the material was simulated by element birth/activation technique, in which all the elements of the finished part are deactivated at first. Godak's weld source (more details in 2.3) heats the elements and activates them thermally within the temperature range of 1200°C - 1210°C. This range was chosen because a specific temperature value can provoke convergence problems.

As the thermal properties, the structural properties also remain in quiet or death state at the start of the simulation. For it, the specific thermo-elastic-plastic model ***MAT_CWM 270** based on Von-Mises yield criteria and kinematic hardening is used. In the quiet or death state, the material properties feature a Poisson's ratio (0.45), Young's modulus (1000 N/mm²), heat capacity (4.3E mJ/tonK), thermal conductivity (0.001 mW/mm°C) thermal expansion (0 mm/°C) [14]. These dead elements are activated when the temperature exceeds the melting temperature in the range of 1400°C – 1450°C. This makes sure, that the thermal material properties and conditions (see 2.4) are activated before the structural analysis starts [14]. Activated and deactivated elements can deform in the structure, but deactivated elements are nearly without mechanical properties.

Temperature-dependent material properties such as Young's modulus, Poisson's ratio, yield strength, coefficient of thermal expansion etc. were taken from [13,14].

The graphs in *Fig.2* show the properties of the temperature dependent material. With increasing temperature, the Young's modulus decreases up to the melting temperature and becomes almost zero. Similarly, the yield stress and the hardening modulus decrease with increasing temperature. The Poisson ratio increases as the young's modulus decreases with temperature. On the other hand, the convection and radiation increase at higher temperatures. The combined value of convection and radiation is adopted from [14].
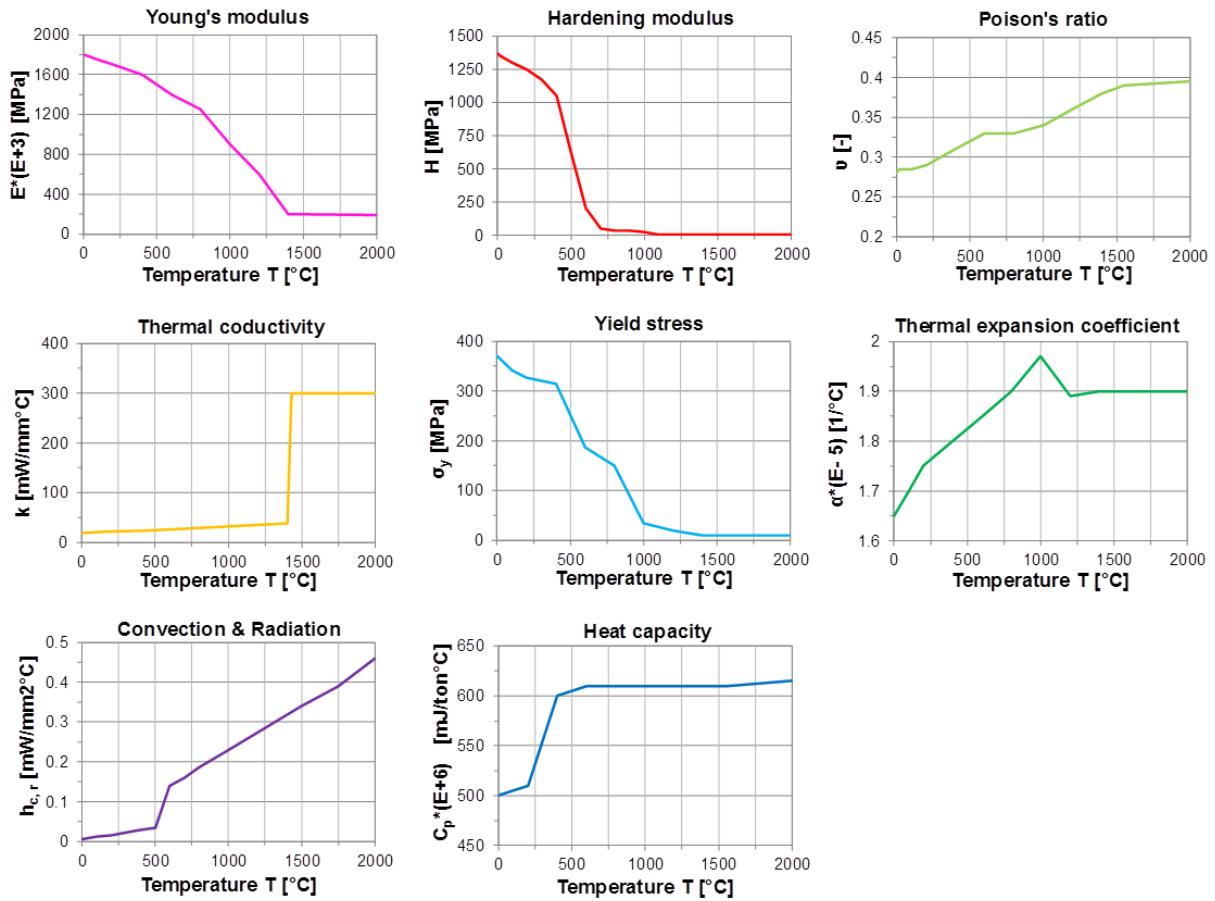
Fig.2: *Mechanical and thermal material properties for steel [13,14]*

2.3 Parameters of the Goldak's weld heat source

Godak's weld heat source model (***BOUNDARY_THERMAL_WELD_TRAJECTORY)**, based on Gaussian power density distribution in space, was used as boundary condition. The heat source distribution pattern in this model is shown in *Fig.3*. For a double ellipsoidal heat source, the parameters and their corresponding values used in this work are given in Table 1. The parameters a, V, I, Q and v are based on own experiments and c, f and n are choosen in accordance with [15].The feed of the welding torch is 7.5 mm/s.

Table 1: Goldak's ellipsoidal parameters
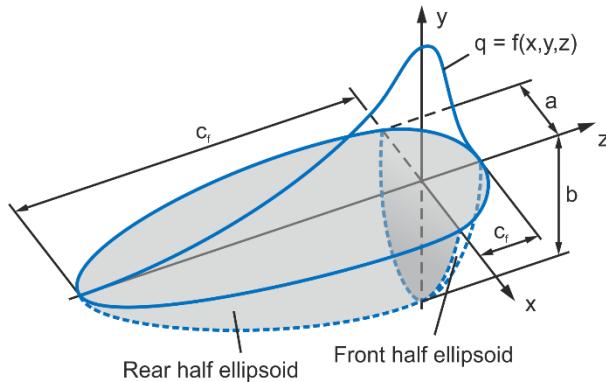
Fig.3: *Goldak's heat source distribution pattern [16]*

Weld pool width	**a**	2.25 mm
Weld pool depth	**b**	1.6 mm
Forward weld pool	**c_f**	2.5 mm
Rearward weld pool	**c_r**	5.0 mm
Forward heat factor	**f_f**	1.0
Rearward heat factor	**f_r**	1.0
Exponent constant	**n**	1.0
Welding voltage	**V**	23 Volt
Welding current	**I**	80 Ampere
Weld pool energy	**Q**	1.84E6 mW
Heat source velocity	**v**	7.5 mm/s

The distribution of the energy within Goldak's moving heat source model in Cartesian coordinate system is given by the Eq.1 and Eq.2 [17].

$$q_f(x,y,z) = \frac{2nf_f\sqrt{n}Q}{\pi\sqrt{\pi}a_f b_f c_f}e^{-n\left(\frac{x}{a}\right)^2}e^{-n\left(\frac{y}{b}\right)^2}e^{-n\left(\frac{z}{c_f}\right)^2} \tag{1}$$

$$q_r(x,y,z) = \frac{2nf_r\sqrt{n}Q}{\pi\sqrt{\pi}a_r b_r c_r}e^{-n\left(\frac{x}{a}\right)^2}e^{-n\left(\frac{y}{b}\right)^2}e^{-n\left(\frac{z}{c_r}\right)^2} \tag{2}$$

The weld pool energy is expressed by

$$Q = \eta UI \tag{3}$$

where the efficiency of the arc, is the arc voltage and is the welding current. The value of is set to 1. Generally, the sum of both heat factors should be equal to 2. The temperature peak of Goldak's distribution depends on the weld pool energy and the thermal material properties.

$$f_f + f_r = 2 \tag{4}$$

2.4 Contact and activation of boundary conditions

The heat flow during welding is influenced by the convection and radiation at all surfaces exposed to air and conduction takes place along the activated beads and the support. With the expounded parameters, a welding temperature of approximately 1600°C is calculated. After the heat source has passed, the thermal and mechanical behavior of the elements within one bead are activated (*Fig.4*). Every weld bead is defined as a part with tied contact and time-dependent activated thermal contact. Due to thermal contact between the activated beads, the boundary condition convection is deactivated. The surrounding air temperature was set as 50°C, while the inactive parts were considered to be at 20°C.
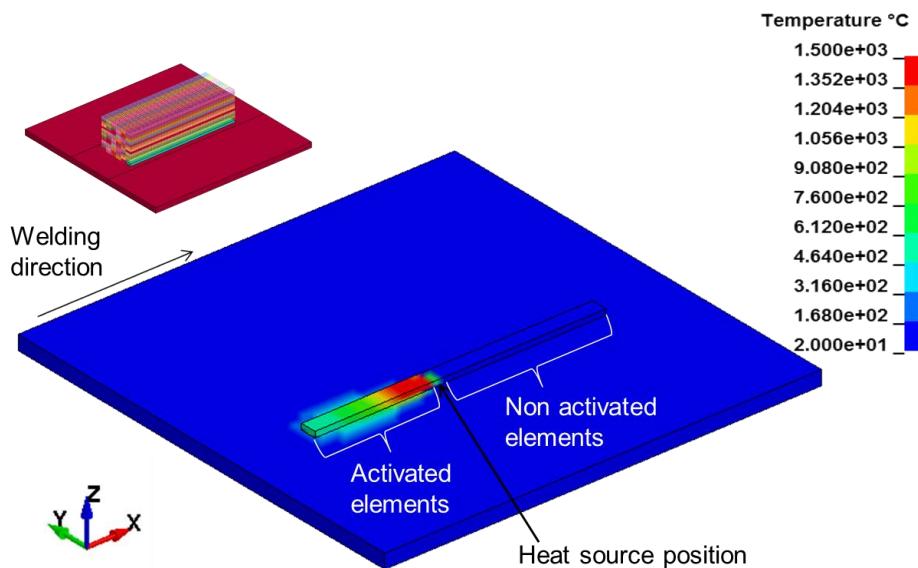
Fig.4:   Activated and non-activated elements within a bead

A mechanical tied contact among all beads which are next to each other has been established before the welding simulation of the first bead starts. This tied surface to surface contact (***CONTACT_TIED_SURFACE_TO_SURFACE_CONSTRAINED_OFFSET**) remains active during the process. ***CONTACT_AUTOMATIC_SURFACE_TO_SURFACE_THERMAL** was used for thermal contact between the beads laying parallel to each other and above/below each other. As it is impossible to activate criterion-based thermal contact, the changing thermal conditions between the ropes were predetermined according to the time, i.e., the thermal contact between the surfaces will become active at specific times. The boundary conditions for convection and radiation was coupled in the thermal contacts in such a way, that as the contact between the two surfaces becomes active, the convection and radiation will be stopped (**BCFLG=1**).
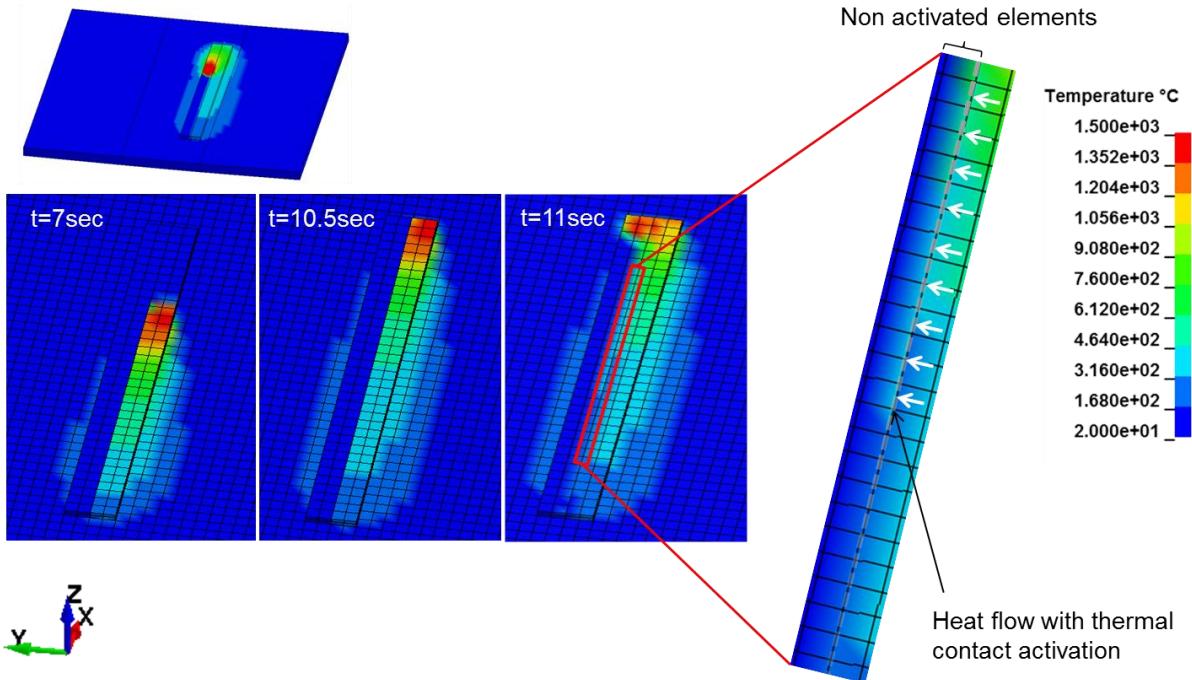
Fig.5: Heat flow with thermal contact activation

When thermal contacts are activated for a bead, heat flow occurs between the contact surfaces regardless of the actual activation of the elements. This can be seen in (*Fig.5*) where at a time of 11 sec a heat flux into the deactivated elements within an activated bead can be detected. For the welding speed used in these investigations, the error is negligible because the temperature rises to about 300°C and does not activate the properties. Further, this undesirable effect does not influence the global thermal household. There is no option available in LS-DYNA to activate the contacts element-wise currently. To minimize this effect on larger and complex models, the sub-division of the beads is recommended.

With reference to [14] the convection and radiation temperature dependent values of the heat transfer coefficient were used as one convection condition ***BOUNDARY_CONVECTION_SET**. The conduction between the surfaces follows the equation of heat conduction for welding [18] and is given as:

$$ \tag{5} $$

Here is the gradient operator, is the density of the material, is the specific heat, is the rate of (internal) heat generation per unit volume, k is the thermal conductivity, T is the temperature, and is the velocity.

A cooling simulation for two test cases has been carried out to validate the boundary conditions for the heat (*Fig.6*). In simulation A, only the outer surfaces of the box were chosen for convection and radiation while in simulation B the surfaces were selected automatically by the contact option **BCFLG = 1**. It was observed that the cooling curves for both simulations were almost the same with the maximum difference in the temperature (ΔT_{max}) of about 15°C.
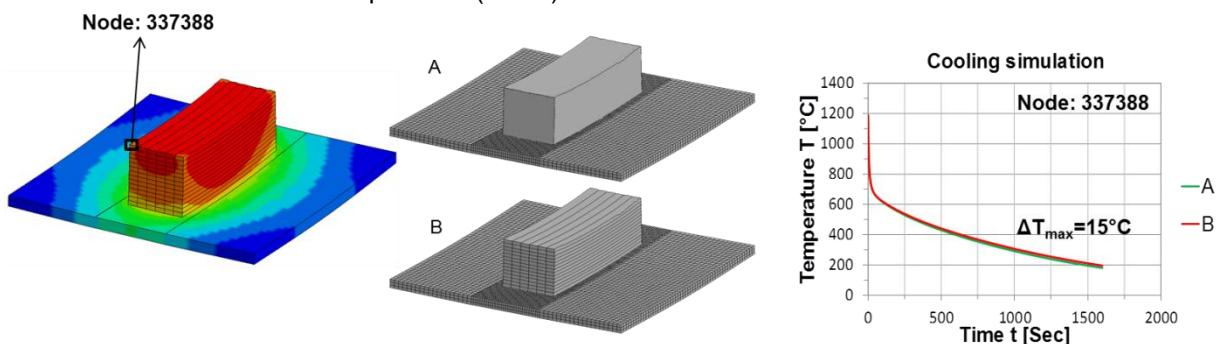
Fig.6: Cooling simulation for (A) with convection from the outer surfaces of the box, (B) using BCFLG = 1 to deselect surfaces with mechanical contact

2.5 Solver settings of the coupled structural thermal analysis

To solve the nonlinear thermal-structural problem with material properties evaluated at 8 gauss points for temperature, the implicit symmetric direct solver (double precision R101) was employed. A constant time step of 0.125 sec was kept for the welding simulation (900 sec), whereas in the cooling simulation the time step was increased to 5 sec and 50 sec respectively as shown in *Fig.7*. For the mechanical calculation, the implicit solver uses an automatically adjusted time step size with the same values as the thermal solver for the maximum allowable time step size. To obtain extended information for the first bead and layer, even the frequency of outputs is changed according the simulation sections. Hourglass control (type Belytschko-Bindeman) is used, which assumes a strain co-rotational stiffness form for 3D solid elements (QM = 0.1).
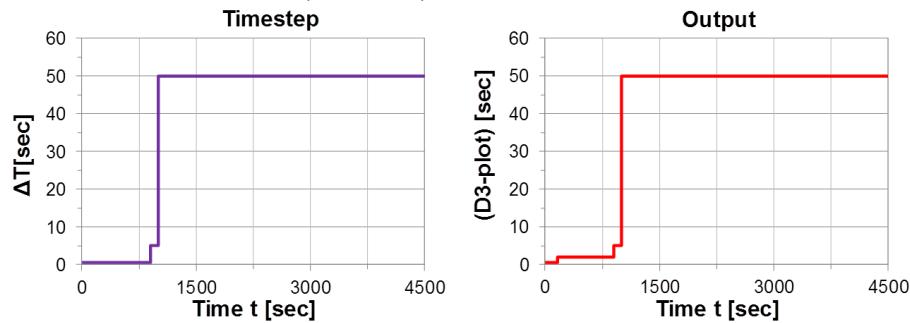
Fig.7:   *Time step and output interval size for thermal and mechanical simulation*

3 Simulations for different path strategies

In this work four welding path strategies were investigated as shown in *Fig.8*. The strategies include beads lying bi-directional (V1), uni-directional (V2), crosswise (V3) and from outside to inside in a spiral form with alternate start positions in each layer (V4). As mentioned before, the boxes feature 14 layers, 88938 elements of fully integrated S/R solid elements (**ELFORM = –1**), but different amounts of beads. Welding strategies V1 and V2 exhibit with 84 beads minimal numbers of beads. V3 exhibit 168 and V4 154 beads.
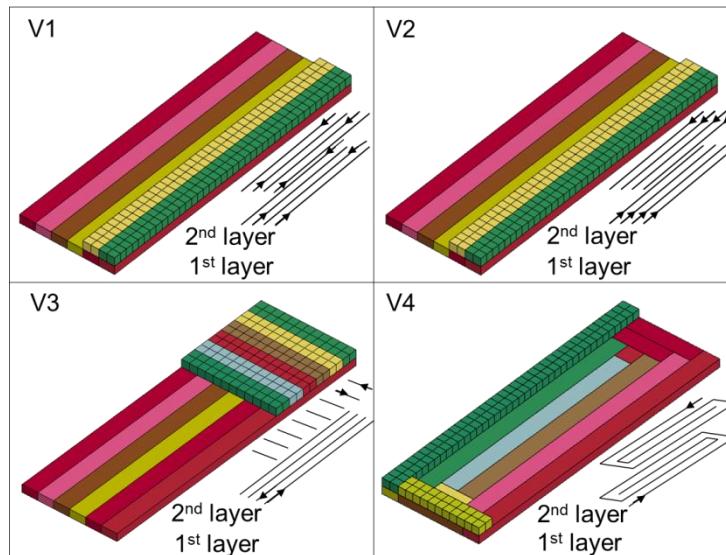
Fig.8:   *Different path strategies implemented for WAAM process simulation with parallel paths bi-directional (V1), uni-directional (V2), crosswise (V3) and in a spiral form (V4)*

The distribution of Von-Mises stresses and effective plastic strains after welding simulation (900 sec) and after cooling simulation (4500 sec) are shown in *Fig.9*.
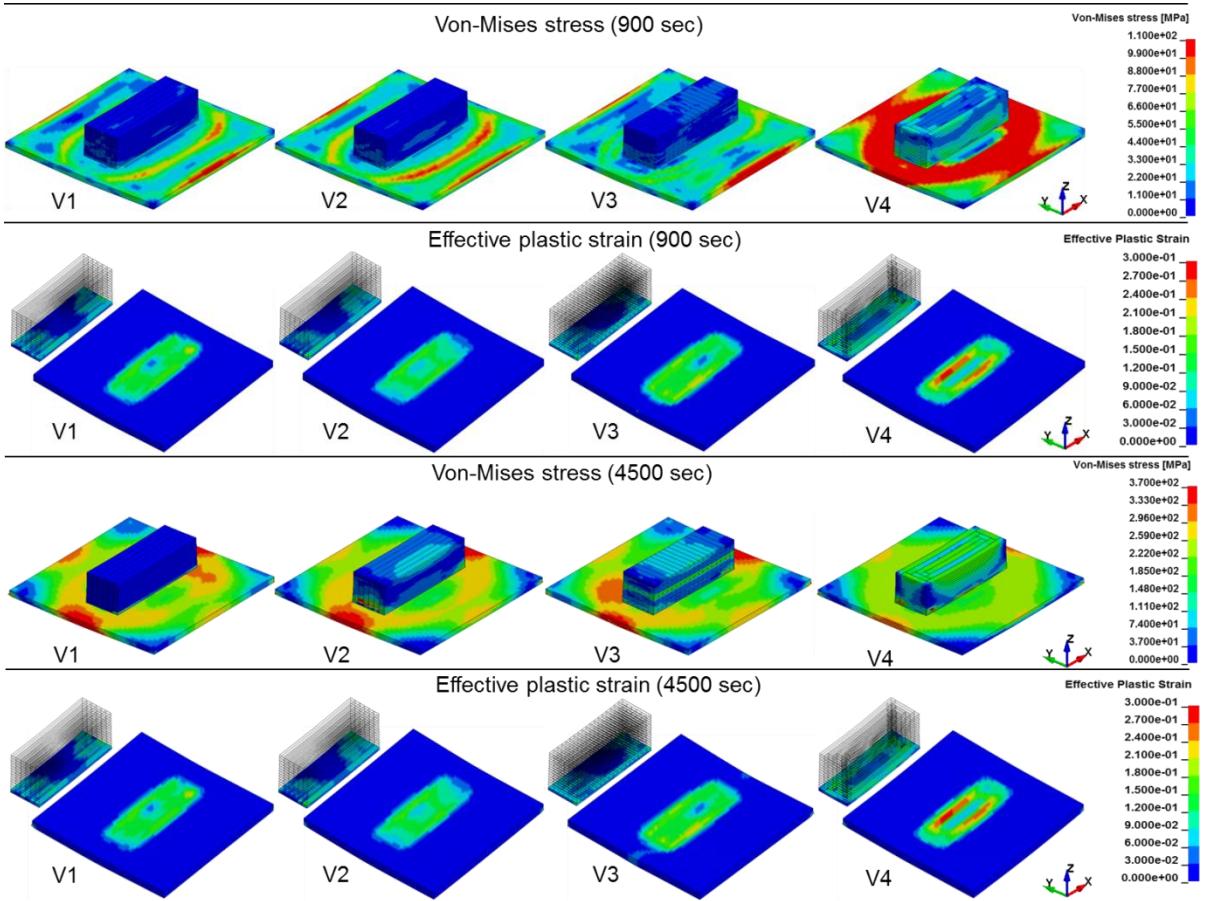
Fig.9: Von-Mises stress and effective plastic strain distribution after welding (t = 900 sec) and cooling (t=4500 sec) simulation

All four strategies show two global effects, a ring-shaped deflection around the welded box and a distortion at the edges. Directly after welding (900 sec), for the area of the ring-shaped deflection a temperature of 800°C and at the edges of 750°C are calculated, which correpsonds to a yield stress of approximately 80N/mm². After a process time of 4500 sec in the ring-shaped deflection and the edges nearly room temperature (35-45°C) is reached with a yield stress of 370N/mm².

The greatest ring-shaped deflection occurs in V4 and the greatest distortion at the edges in V2. To interpret these results, it should be mentioned again, that the support plate can slide and expand almost freely. So it is coherent that the V1, which starts welding on one side with alternating directions, shows moderate stresses in the ring-shaped deflection zone and distortion of the edges directly after welding. Parallel beads in the same direction (V2) conform to a discontinuous path which leads to a higher stress in the ring-shaped deflection and a less distortion of the edges. As a result of the crosswise pattern in V3, the stresses of the ring-shaped deflection can be reduced remarkably, but on the other hand the deflection of the edge increases. Strategy V4 heats at first the complete outer contour of the box, with leads to maximum stresses and even to an exceedingly high effective plastic strain distribution.

For this small benchmark-box the effective plastic strains in the first layer are coupled with the position and direction of the start beads and do not change significantly during the cooling procedure. This leads to the conclusion, that the crack tendency for WAAM-processes without a time delay between ropes and layers is defined by the path strategy of the first two layers.

As expected, during the cooling process the residual stresses increase up to the yield stress at room temperature. As a consequence, elastic-plastic deformations occur, but the plastic portion compared with deformation during welding is negligible.
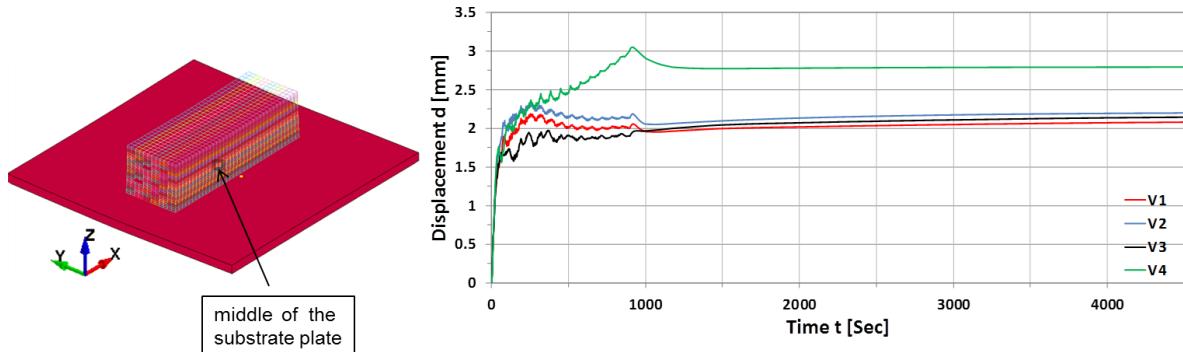
Fig.10: Resultant displacement in the middle of the substrate plate

The position of maximum deformation is nearly in the middle of the support, but changes with the strategies (*Fig.10*). In strategy V4 the largets displacement of about 3 mm takes place at the end of the welding process (900 sec). The deformation pattern of V1 and V2 is found to be almost the same at about 250 sec. V3 shows less deformation of approximately 2 mm.

The deformation behavior of the object during welding depends highly on the fixation of the support, the material properties and the path strategy. In *Fig.11* the geometries after cooling are shown.
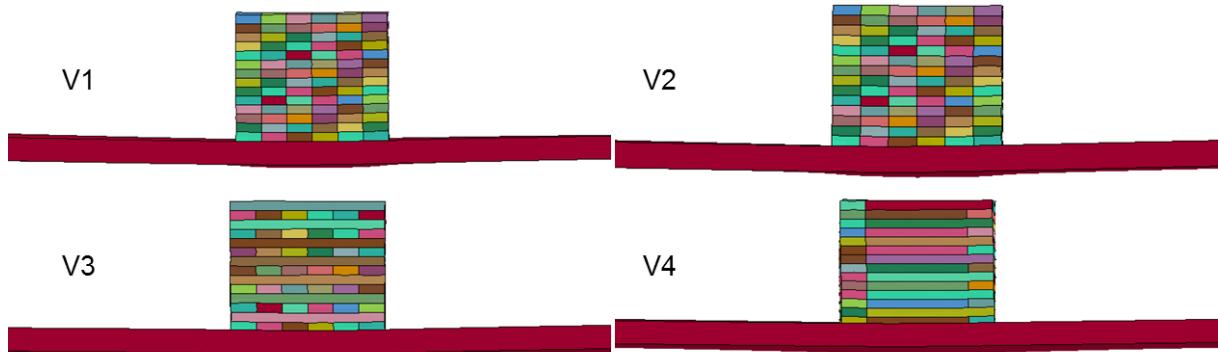
Fig.11: Deformation pattern of substrate-plates

4 Summary

Wire-Arc additive manufacturing was considered in this work to simulate a box-shaped part using different strategies. The thermo-mechanical analysis was performed with temperature-dependent material properties of 309L steel and Goldak's heat source model. Moving local temperature peaks cause a development of stresses and strains in the structure and leads to deflection and distortion of the support plate.

The stress distribution and effective plastic strains after welding (900 sec) and cooling (4500 sec) are shown for four welding strategies. The comparison of the strategies is carried out for a ring-shaped deflection around the box, the distortion at the edges and the displacement of the substrate plate. Overall the crosswise pattern features a minimum of unwanted effects. This statement depends highly on the discussed model and may change with other boundary conditions.

In the future, the development of microstructure and residual stresses for different strategies for the welding and cooling simulation will be analyzed and the path-planning tool for thin structures [19] will be adapted to a preprossesor for WAAM-simulations.

5 Acknowledgment

References

[1]   Williams SW, Martina F, Addison AC, Ding J, Pardal G, Colegrove P. Wire + Arc Additive Manufacturing. Materials Science and Technology 2015;32(7):641–7.

[2]   Szost BA, Terzi S, Martina F, Boisselier D, Prytuliak A, Pirling T et al. A comparative study of additive manufacturing techniques: Residual stress and microstructural analysis of CLAD and WAAM printed Ti–6Al–4V components. Materials & Design 2016;89:559–67.

[3]   Ding D, Pan Z, Cuiuri D, Li H. Wire-feed additive manufacturing of metal components: Technologies, developments and future interests. Int J Adv Manuf Technol 2015;81(1-4):465–81.

[4]   Liou Fea. Multiscale and Multiphysics Modeling of Additive Manufacturing of Advanced Materials. Washington, DC; 2015.

[5]   M. Ito, S. Izawa, Fukunishi and M. Shigeta (ed.). SPH Simulation of Gas Arc Welding Process. Japan; 2012.

[6]   Das R, Cleary PW. Three-dimensional modelling of coupled flow dynamics, heat transfer and residual stress generation in arc welding processes using the mesh-free SPH method. Journal of Computational Science 2016;16:200–16.

[7]   Busachi A, Erkoyuncu J, Colegrove P, Martina F, Ding J. Designing a WAAM Based Manufacturing System for Defence Applications. Procedia CIRP 2015;37:48–53.

[8]   Chiumenti M, Cervera M, Salmi A, Agelet de Saracibar C, Dialami N, Matsui K. Finite element modeling of multi-pass welding and shaped metal deposition processes. Computer Methods in Applied Mechanics and Engineering 2010;199(37-40):2343–59.

[9]   Milan Kucharik, Richard Liska, Pavel Vachal and Mikhail Shashkov. Arbitrary Lagrangian-Eulerian (ALE) methods in compressible fluid dynamics: Programs and Algorithms of Numerical Mathematics 13 2006:178--183.

[10] Bellet M, Hamide M. Direct modeling of material deposit and identification of energy transfer in gas metal arc welding. Int Jnl of Num Meth for HFF 2013;23(8):1340–55.

[11] Ding J, Colegrove P, Mehnen J, Ganguly S, Sequeira Almeida PM, Wang F et al. Thermo-mechanical analysis of Wire and Arc Additive Layer Manufacturing process on large multi-layer parts. Computational Materials Science 2011.

[12] Klusemann B, Bambach M. Stability of phase transformation models for Ti-6Al-4V under cyclic thermal loading imposed during laser metal deposition. In: PROCEEDINGS OF THE 21ST INTERNATIONAL ESAFORM CONFERENCE ON MATERIAL FORMING: ESAFORM 2018. Author(s); 2018, p. 140012.

[13] Nadimi S, Khoushehmehr RJ, Rohani B, Mostafapour A. Investigation and Analysis of Weld Induced Residual Stresses in Two Dissimilar Pipes by Finite Element Modeling. J. of Applied Sciences 2008;8(6):1014–20.

[14] Lindström P. Improved CWM platform for modelling welding procedures and their effects on structural behaviour. Trollhättan: University West; 2015.

[15] Bhusan Prasad B. Simulation of heat source in gas metal arc welding by using LS-PrePost (Tutorial), 2018:1-32.

[16] Jia X, Xu J, Liu Z, Huang S, Fan Y, Sun Z. A new method to estimate heat source parameters in gas metal arc welding simulation process. Fusion Engineering and Design 2014;89(1):40–8.

[17] Goldak J, Bibby M, Moore J, House R, Patel B. Computer modeling of heat flow in welds. Metallurgical Transactions B 1986;17(3):587–600.

[18] Yadaiah N, Bag S. Effect of Heat Source Parameters in Thermal and Mechanical Analysis of Linear GTA Welding Process. ISIJ Int. 2012;52(11):2069–75.

[19] NGUYEN L, BUHL J, Bambach M. DECOMPOSITION ALGORITHM FOR TOOL PATH PLANNING FOR WIRE-ARC ADDITIVE MANUFACTURING. Journal of Machine Engineering 2018;Vol.18(No.1):96–107.